NJC

ROYAL SOCIETY OF CHEMISTRY

PAPER

View Article Online
View Journal | View Issue

Cite this: *New J. Chem.*, 2023, **47**, 6235

Exploring the electrochemical characteristics of the nucleobase-template assisted $NiCo_2O_4$ electrode for supercapacitors†

Karthik Krishnan, *[a] Amuthan Dekshinamoorthy,[a] Saranyan Vijayaraghavan[a] and Selvakumar Karuthapandi *[b]

Metal–nucleobase nanostructures are considered essential electrode materials in demonstrating the electrochemical performance of supercapacitors for energy storage devices. In this study, different combinations of nucleobases have been used as metal coordination ligands to prepare the $NiCo_2O_4$ (NCO) nanostructures. Of specific interest, the nucleobases such as adenine (A), guanine (G), and cytosine (C) were used in different combinations such as A–G, A–C, and G–C for modulating the structure and morphology of NCO. Owing to the synergistic effect of higher electronic conductivity and sheet-like morphology, the NCO/A–G obtained from the Ni–Co/A–G complex shows enhanced supercapacitance characteristics relative to that of the NCO nanostructures obtained using other combinations (A–C and G–C). In particular, the NCO/A–G as an electrode material shows a maximum specific capacity of ~130 mA h g^{-1} at a current density of 0.3 A g^{-1}. Significantly, the fabricated asymmetric supercapacitor (ASC) consisting of six-series cells extends the operating voltage of 6.5 V with good energy and power density of 8.5 μW h cm^{-2} and 400 μW cm^{-2}, respectively. It is also demonstrated that the NCO/A–G-based supercapacitor effectively lights up a blue light-emitting diode for a certain time, suggesting the feasibility of morphologically tuned nucleobase–metal complexes for practical energy storage devices.

Received 5th November 2022,
Accepted 21st February 2023

DOI: 10.1039/d2nj05436a

rsc.li/njc

1. Introduction

An investigation of electrode materials and the corresponding electrochemical energy storage characteristics plays a crucial role in developing next-generation energy storage devices.[1–3] Due to its high power density, fast charge–discharge rate, and large capacitance characteristics, the supercapacitor is considered an essential candidate for energy storage devices in both stationary and mobile applications.[4,5] In principle, charge storage in the electrode material can occur either electrostatically (electrical double layer [EDL] formation) or electrochemically (pseudo-capacitance) under biasing conditions.[6,7] In electric double-layer capacitors (EDLCs), the electrostatic interaction between the ionic charges at the electrode/electrolyte interface forms the EDL by the adsorption/desorption of ionic carriers.[8] The EDLC performance mostly relies on the types of electrode material and its properties such as surface area, morphology, electrical conductivity, *etc.*[9–11] In general, downscaling of materials to the characteristic nanoscale offers a large surface area, which promises for achieving higher power and energy densities relative to that of the bulk-scaled materials with the same chemical composition.[12,13]

In recent years, transition metal oxides such as zinc oxide (ZnO), vanadium oxide (V_2O_5), cobalt oxide (Co_3O_4), ruthenium oxide (RuO_2), and other related materials have been extensively employed as electrode materials for supercapacitors.[14–25] Among the widely studied supercapacitor electrode materials, a spinal structure (AB_2O_4) of mixed transition metal oxides, comprising single-phase ternary metal oxides with two various transition metal elements has attracted much attention because of its higher electronic conductivity and electrochemical activity than the single transition metal oxides.[26–28] In particular, spinel nickel cobaltite ($NiCo_2O_4$ [NCO]) has been broadly investigated as an electrode material in EDLC because of its advantages including large theoretical capacitance value (≥3000 F g^{-1}), low cost, environmental-friendliness, *etc.*[29,30] However, the practical capacitance of NCO is much lower than the theoretical capacitance value, interpreted by limited surface area and relatively poor conductivity.[31] In order to enhance the practical capacitance characteristics, numerous investigations have been done with various strategies including optimization of specific surface area,

[a] *Corrosion and Material Protection Division, CSIR-Central Electrochemical Research Institute, Karaikudi, Tamil Nadu 630003, India. E-mail: karthikk@cecri.res.in*
[b] *Department of Chemistry, School of Advanced Sciences, VIT-AP University, Amaravati, Andhra Pradesh 522237, India. E-mail: selvakumar.k@vitap.ac.in*

† Electronic supplementary information (ESI) available. See DOI: https://doi.org/10.1039/d2nj05436a

particle size and shape controllability, enhancement of oxygen vacancies, and incorporation of a small amount of impurities into the NCO.[32–34] It is well-known that the particle size, morphology, and specific surface area of the nanostructured inorganic electrode materials can play a vital role in the electrochemical properties; therefore, it is highly desirable to select an appropriate metal coordination ligand to modulate the electrochemical properties of electrode materials.[35,36] Coordination of organic ligands to metal centres has been known to assist the nanoscale architectures of metal oxide-based electrodes. Hu *et al.* have shown the use of imidazolate ligands (*e.g.*, zeolitic imidazolate framework-67 (ZIF-67)) to synthesize $Co_3O_4/NiCo_2O_4$ double-shelled nanocages displaying enhanced pseudo-capacitance behavior.[35] Gao and co-workers have harnessed the complexation chemistry of Ni^{2+} and Co^{2+} toward citric acid ligands and solvothermal processes to synthesize urchin-like $NiCo_2O_4$ with significant oxygen vacancies and improved capacitance characteristics.[36] The unique aspect of the current work, which distinguishes our work from other work, is the use of nucleobases as coordination ligands which offer greater variability in metal ligand-coordination, as well as in terms of combinatorial possibilities, as compared to the conventional organic ligands.

Here, we report the morphologically tuned NCO nanoparticle with various combinations of nucleobases (adenine–cytosine [A–C], guanine–cytosine [G–C], and adenine–guanine [A–G]) in a hydrothermal synthesis process. The purines (adenine and guanine) and the pyrimidines (cytosine and thymine) are the nucleobases that offer intriguing molecular recognition properties, and are often manipulated to prepare self-assembled supramolecular structures.[37] Their molecular surface not only presents hydrogen bond donor (N–H)/acceptor sites (N and C═O) for self-assembly formation and interaction with protic solvent molecules, but also provides Lewis basic metal coordination sites as depicted in Scheme 1.[38,39] Hence, it is speculated that the metal coordination property of nucleobases in combination with their hydrogen bonding capability and π–π stacking interaction can tune the structure and sheet-like morphology of the NCO nanostructures, which is highly desirable to attain enhanced electrochemical performance.

The NCO nanostructures with three different and well-defined morphologies, including tiny poly-crystals, aggregated poly-crystals, and large sheet-like structures have been prepared by the optimized nucleic acid combinations and reaction conditions.

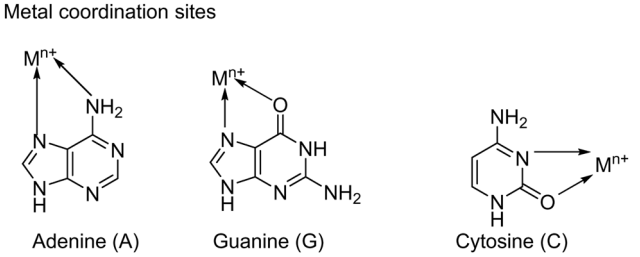

Scheme 1 Illustration of possible metal coordination Lewis base sites in nucleobases.

Tuning of the NCO morphology greatly improves the supercapacitance characteristics, interpreted by various electrochemical studies. Combinations of adenine and guanine-based NCO nanostructures (NCO/A–G) show a maximum specific capacity of 130 mA h g^{-1}, which is relatively higher than the other two NCOs. To demonstrate the supercapacitance characteristics for practical applications, we constructed the all-solid-state ASC comprising an electrolyte (PVA–KOH) sandwiched between the NCO/A–G and the conductive carbon-based electrodes. The ASC consisting of six-series cells exhibits a maximum operating cell voltage (6.5 V) with accumulated energy and power density of 8.5 μW h cm^{-2} and 400 μW cm^{-2}, respectively. To quantitatively analyze the high-performance device characteristics, four series cells were connected with a light-emitting diode (LED) after one complete charging (up to 6 V), which effectively lights up a LED.

2. Experimental section

2.1. Materials

Nickel nitrate hexahydrate ($Ni(NO_3)_2{\cdot}6H_2O$ (Himedia, 98%) and cobalt nitrate hexahydrate ($Co(NO_3)_2{\cdot}6H_2O$ (Himedia, 98%) were used as received. Nucleic acids such as guanine, adenine, and cytosine were used as received from Spectrochem, India. The aqueous solutions were prepared using deionized (DI) water. All these analytical-grade chemical reagents were used without additional purification.

2.2. Synthesis of different $NiCo_2O_4$ nanostructures using nucleic acids

The hydrothermal method was adopted to prepare the $NiCo_2O_4$ nanostructures using different combinations of nucleic acids (G–C, A–C, A–G). In a typical reaction, 1.12 g (3.9 mmol) of $Ni(NO_3)_2{\cdot}6H_2O$, 2.05 g (7.0 mmol) of $Co(NO_3)_2{\cdot}6H_2O$, 0.1 g of guanine (0.7 mmol) and 0.1 g of cytosine (0.9 mmol) were dissolved in 100 mL of DI water. The reaction mixture was constantly stirred for 30 min to obtain a homogeneous solution. Then, the homogeneous solution was transferred into a 100 mL Teflon-sealed stainless autoclave. The autoclave was kept inside the high-temperature furnace and maintained at 150 °C for 6 h. After it was cooled to room temperature, the product was washed several times with DI water and ethanol. The final product was calcined at 500 °C for 6 h in an air atmosphere. The prepared $NiCo_2O_4$ nanopowders with guanine and cytosine were labeled as NCO/G–C. Similarly, the NCO/A–C and NCO/A–G were prepared with adenine : cytosine (0.1 : 0.1 g) and adenine : guanine (0.1 : 0.1 g), respectively. The schematic representation of the synthesis procedures for the Ni–Co/nucleobase complexes and the subsequent transformation of these complexes into the NCO electrode is shown in Fig. 1.

2.3. Material characterization

The crystal structure of the prepared NCO nanostructures was characterized using an X-ray diffractometer (XRD; X'Pert PRO, PANalytical, Cu Kα, λ = 0.15406 nm). The morphology and structural information of the prepared samples were examined

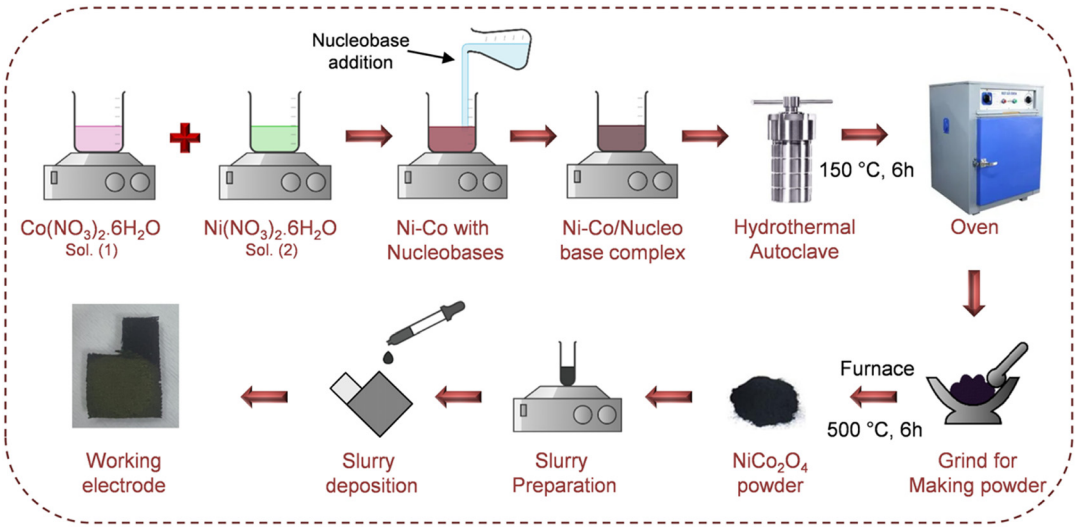

Fig. 1 Schematic representation of the synthesis procedures of NCO–nucleobase complexes and the preparation of the NCO-based working electrode.

using scanning electron microscopy (SEM; JEOL JSM-6700F, 5 kV), and high-resolution transmission electron microscopy (HRTEM; JEOL, JEM-2010 HT). Brunauer–Emmett–Teller surface areas and pore volumes were measured using Quantachrome instruments with nitrogen adsorption at 77 K.

2.4. Electrochemical measurements

The electrochemical measurements were initially carried out in a three-electrode configuration using an electrochemical workstation (Metrohm Autolab potentiostat/galvanostat instruments) at room temperature and ambient conditions. The three-electrode measurement was done in a 3 M KOH aqueous electrolyte. Prior to preparing the electrode materials, the carbon cloth (1 cm × 1 cm) was cleaned with acetone, DI water, and ethanol. For drying, the cleaned carbon cloth was kept at 70 °C for approximately 5 h. In a three-electrode configuration, the platinum (Pt) wire was used as a counter electrode, the saturated calomel electrode (SCE) was used as a reference, and the prepared NCO was used as the working electrode. The working electrode was prepared by mixing the NCO (80 wt%), carbon black Super-P (10 wt%, TIMCAL-ThermoFisher Scientific, India), and polytetrafluoroethylene (PTFE) (10 wt%) in *N*-methyl pyrrolidinone (NMP) solvent to form a homogeneous slurry. Then the prepared slurry was uniformly coated on the carbon cloth surface with an NCO loading of around 2.0 mg cm^{-2} and kept at 70 °C overnight before carrying out the cyclic voltammetry (CV), galvanostatic charging/discharging (GCD), and electrochemical impedance spectroscopy (EIS) measurements with different scan rates and current densities.[40,41]

2.5. ASC fabrication

The all-solid-state ASC was fabricated using the prepared NCO as the cathode and the carbon black super-P coated carbon cloth as the anode. In order to fabricate the ASC device, the polyvinyl alcohol (PVA)–potassium hydroxide (KOH) electrolyte was sandwiched between the cathode and the anode with a dimension of 1 cm × 1 cm. Then, the fabricated ASC device was dried overnight at 80 °C. For the PVA–KOH electrolyte, 1 g of PVA was dissolved in 15 mL of DI water with continuous stirring at 90 °C for 2 h. Then, 1g of KOH was dissolved separately in 5 mL of DI water and added to the PVA solution. After 15 min, the homogeneous PVA–KOH mixture was transferred into the glass Petri dish and maintained at 60 °C for 12 h. Finally, the PVA–KOH film was peeled-off from the Petri dish for the $NiCo_2O_4$-based ASC device.

In the CV studies, the cyclic sweep rate was varied between 1 and 100 mV s^{-1}. In the GCD studies, the device was charged and discharged with different charge–discharge current densities. The areal capacitance and specific capacity were calculated using eqn (1) and (2), respectively,

$$C_a = I \times \Delta t/(S \times \Delta V) \quad (1)$$

$$C = I \times \Delta t/m \quad (2)$$

where C_a and C represent areal capacitance and specific capacity, respectively. I, S, and m are the constant discharge current, geometric area of the electrode, and loaded metal mass (mg), respectively. Δt (t) and ΔV (V) are the discharge time and potential drop during discharge, respectively. The energy density (E_d, mW h cm^{-2}) and power density (P_d, mW cm^{-2}) of the supercapacitor device are evaluated using the following relation,

$$E_d = (C_s \times \Delta V^2)/2 \quad (3)$$

$$P_d = E_d/\Delta t \quad (4)$$

where C_s is the specific capacitance, ΔV (V) is the potential window and Δt (t) is the discharge time, respectively.

3. Results and discussion

3.1. Crystalline structure of the prepared NCO–nucleobase electrode materials

The crystalline structure of the prepared NCOs was determined using powder X-ray diffraction (XRD) analysis. Fig. 2 represents the XRD patterns of the NCO powders with various combinations of nucleobases in them. The observed major peaks of NCO powders indicate the presence of a cubic spinel phase, which is well matched with the standard Joint Committee on Powder Diffraction Standards (JCPDS no. 20-0781).[42] The peak positions were found to be 18.9°, 31.2°, 36.8°, 44.3°, 55.2°, 59.1°, and 64.9°, corresponding to the (1 1 1), (2 2 0), (3 1 1), (4 0 0), (4 2 2), (5 1 1), and (4 4 0) planes.[43] From the XRD patterns, the formation of a cubic spinel phase with the *F*3*dm* space group is existing in all the samples.[44]

Note that, all three samples show similar peaks with higher peak intensity in the XRD profile revealing that the NCOs are crystalline in nature.[45,46] The NCO/G–C powders show relatively higher crystalline ordering as compared to that of the remaining two samples. Moreover, the obvious peak broadening in the XRD pattern is ascribed to the formation of nano-crystalline ordering in the prepared powder. The average particle sizes of the NCOs such as NCO/G–C, NCO/A–C, and NCO/A–G were estimated to be ~12 nm, ~16 nm, and ~19 nm, respectively. The difference in particle size from one sample to another can be due to the influences of various combinations of nucleobases during NCO preparation.

3.2. Morphological and structural analysis of the NCO–nucleobase electrode materials

The morphological and structural features of the prepared NCO/G–C, NCO/A–C, and NCO/A–G were studied using SEM, transmission electron microscopy, and selected area electron diffraction (SAED) patterns. Fig. 3a–f shows the SEM images of the prepared NCOs with different nucleobase combinations. From Fig. 3(a, d), and (b, e), the morphology of NCO/G–C and NCO/A–C appears as nanometer-size aggregates with an average size ranging from 50 to 100 nm. The formed nanostructures can be due to the aggregation of crumbled flake-like structures during the hydrothermal reaction, in which the nucleobases along with metal ions majorly contributed for originating the nuclei formation. The complete crumbling of the sheet morphology in the NCO/G–C could be associated with the lack of adenine coordination ligand in the precursor of the Ni–Co/G–C complex used for the calcination. Fig. 3c and f show the SEM images of the NCO/A–G with different magnifications. It can be clearly seen that the sheet-like morphology is predominant in this case, which is in contrast to the morphological features of the other two NCO nanostructures. It is essential to mention that the sheet-like morphology with large voids appeared on the entire surface of the NCO/A–G. The combinatorics clearly indicate that the metal coordination properties of adenine and guanine and their intermolecular interaction in the Ni–Co/A–G complex play a synergistic role in the emergence of the sheet-like morphology in the NCO/A–G. As seen in the previous section (Scheme 1), the number of Lewis base coordination sites in the molecular structure of purines (A and G) is more as compared to pyrimidine base (C). Furthermore, the number of hydrogen bonding acceptors is relatively more in (A and G) as compared to (C).

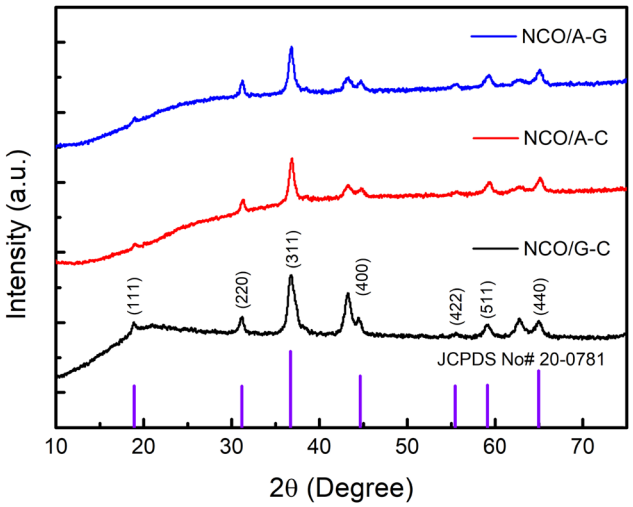

Fig. 2 XRD patterns of the prepared NCO–nucleobase electrode materials.

In order to elucidate deeper insight into the morphological characteristics, both TEM and HRTEM analyses were carried out. Fig. 4a–c represents the TEM images of the NCO/G–C, NCO/A–C, and NCO/A–G nanostructures, respectively. Fig. 4d–f and g–i are the corresponding HRTEM images and SAED patterns, respectively. It is significant that the particles are distributed uniformly in both NCO/G–C and NCO/A–C, whereas the sheet-like morphology appeared in the NCO/A–G. From the HRTEM images, the average particle size is found to be approximately 15 and 20 nm for NCO/G–C and NCO/A–C, respectively; which is in agreement with the estimated particle size from the Debye–Scherrer relation using XRD patterns. Despite large variations in the metal coordination properties of adenine and guanine, the NCO/A–G complex exhibits a completely different morphology as compared to the remaining samples. The SAED patterns additionally reveal the structural characteristics of the prepared samples. The ring and dot patterns in the SAED pattern validate the crystallinity of the samples. The SAED patterns of the NCO nanostructures (Fig. 4g–i) are indexed to the (111), (220), (311), and (400) planes of spinel-structured NCO, which is consistent with the results obtained from XRD data. The crystalline nature of the electrode material is desirable for supercapacitor applications, which could provide structure retention for long-term stability.[47,48] Based on these results, the higher distribution of sheet-like morphology with porous structure is dominant in the NCO/A–G. The porous nature of the materials was further confirmed with Brunauer–Emmett–Teller (BET) surface area analysis, as shown in Fig. S1 of the ESI.†[49,50] Based on the BET analysis, the specific surface areas of the NCO/G–C, NCO/A–C, and NCO/A–G nanostructures are found to be 104, 136,

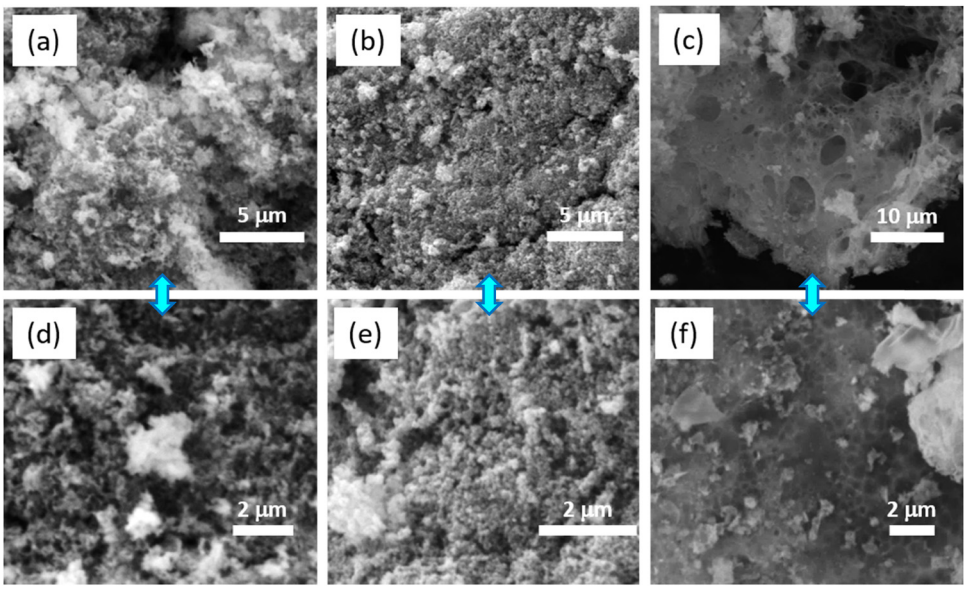

Fig. 3 SEM images of NCO nanostructures using different combinations of nucleic acids, such as (a) G–C, (b) A–C and (c) A–G, and (d–f) are the corresponding magnified images.

and 244 $m^2 g^{-1}$, respectively. In general, the porous structure along with the higher surface area of an electrode material plays a significant role in energy storage applications due to the excellent ionic charge diffusion and the larger contact area of the electrode/electrolyte carriers during redox reactions.

3.3. Electrochemical performance of the NCO-nucleobase electrode materials

To investigate the potential application of NCOs as electrode materials in the supercapacitor, the CV, GCD, and EIS measurements were carried out in a three-electrode configuration with 3 M KOH aqueous electrolyte. At first, the three-electrode-based CV studies have been performed in order to understand the conceivable redox reactions at the electrode/electrolyte interfaces. Fig. 5a and b illustrate the CV curves of the NCO/G–C, NCO/A–C, and NCO/A–G obtained at the sweep rates of 1 mV s^{-1} and 50 mV s^{-1}, respectively. From the CV profiles, it is found that the capacitance characteristics are greatly influenced by the nucleobase combinations, and the scan rates of the CV. A pair of irreversible redox peaks were found in certain sweep rates and fixed potential windows, indicating the existence of the faradaic process similar to the battery behavior.[51,52] By considering the NCO/G–C and NCO/A–C nanostructures, the prominent redox peaks are observed in both forward and reverse sweep cycles (between 1 and 30 mV s^{-1}), as shown in Fig. S2a–d of the ESI.† The observed pseudo-rectangular nature in the CV curve could be due to the redox reactions (oxidation/reduction) of metal ions, *i.e.*, $Ni^{2+} \leftrightarrow Ni^{3+}$ and $Co^{2+} \leftrightarrow Co^{3+} \leftrightarrow Co^{4+}$ on the surfaces of NCO under forward and reverse sweeping conditions.[53] Essentially, the redox behaviors (pseudo-capacitance) tend to transform to a quasi-rectangular shape when the cyclic scan rate is above 50 mV s^{-1}. The origin of the quasi-rectangular shape corresponds to the EDL formation in the cell.[54] Out of the three NCOs, the NCO/A–G shows a quasi-rectangular shape of the CV curves in the entire scan rates (1–100 mV s^{-1}, Fig. S2e and f of ESI†), which is majorly ascribed to the EDL capacitance behavior of the cell. It could also be observed that the separation between the oxidation and reduction peaks does not show an increase in trend with an increase in scan rates, indicating that the NCO/A–G-based electrode is promising for use in ultrafast redox reactions. It is essential to mention that, in the NCO/A–G-based supercapacitor, the current response and shapes of the CV profiles are retained in all the scan rates (1–100 mV s^{-1}), confirming that the sheet-like morphology by the adenine–guanine combination in the NCO evidences better supercapacitance performance relative to that of the remaining two NCO-nucleic acid based cells. Furthermore, the NCO/A–G-based supercapacitor exhibits the largest CV curve integral area (Fig. 5b), which explains the possibility of the highest specific capacity (C). Fig. 5c represents the scan rate-dependent specific capacity (C) plot of the NCOs. In all the cases, the C value increases with the decrease in cyclic scan rate. The higher C value is found to be $\sim$116 mA h g^{-1} for the NCO/A–G-based supercapacitor, whereas the NCO/G–C exhibited a lower value of $\sim$49 mA h g^{-1} at a minimum scan rate of 1 mV s^{-1}.

To further validate the charge–discharge characteristics, GCD measurements have been carried out on all three devices with various current densities in 3 M KOH aqueous electrolyte (potential window: 0–0.45 V). Note that, the discharge behaviors of the NCO-nucleobase electrode-based device are found to possess a capacitive nature, interpreted by almost linear discharge patterns of the cells. Fig. S3 of the ESI† illustrates the GCD profiles of the NCOs studied at various current densities ranging from 0.3 to 4.8 A g^{-1}. The GCD comparison plot between different combinations of nucleobases in the NCO nanostructures is represented in Fig. 5d at a current density of 1.5 A g^{-1}. The storage phenomena and the tendency of charge accumulations designated by the GCD results are closely associated with the CV results. As can be seen in

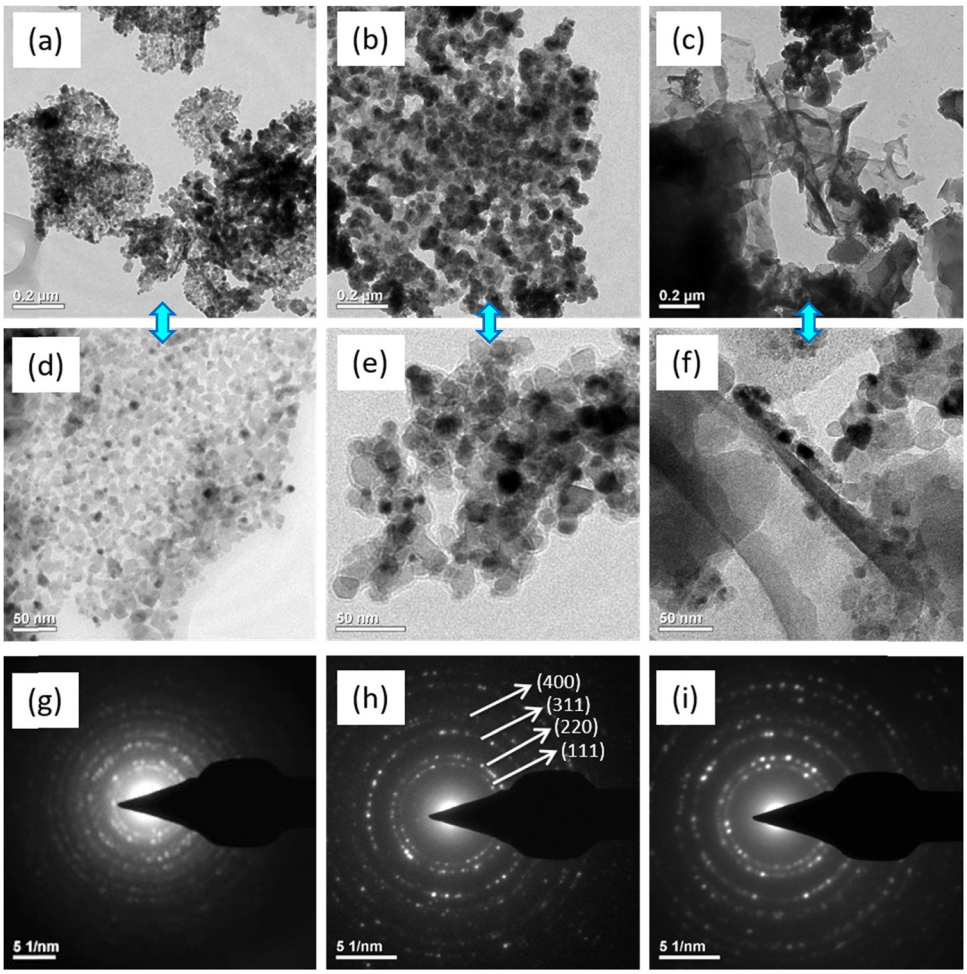

Fig. 4 TEM images of NCO nanostructures using various combinations of nucleic acids, such as (a) G–C, (b) A–C and (c) A–G, and (d–f) are the corresponding HRTEM images; (g–i) SAED patterns of the NCO/G–C, NCO/A–C, and NCO/A–G nanostructures, respectively.

Fig. 5d, the NCO/A–G nanostructure-based cell shows a longer discharge time. To get more information on the long-term cycling capability of the NCO/A–G nanostructure-based cell, the capacitance retention and coulombic efficiency were studied using 7000 continuous GCD cycles at a constant current density of 3.6 A g^{-1} (Fig. S4, ESI†). By using the GCD data, the C values were calculated using eqn (2) at different current densities and the corresponding results are depicted in Fig. 5e. The maximum C values of the NCO/G–C, NCO/A–C, and NCO/A–G nanostructures are found to be 48, 82, and 130 mA h g^{-1} at a current density of 0.3 A g^{-1}, respectively. The NCO/A–G electrode has shown good performance characteristics, which is comparable to the previously reported NCO-based electrodes (Table S1 in ESI†). The improved capacitive performance of the NCO/A–G electrode is attributed to its self-aligned sheet-like morphology with higher porous nature.

Fig. 5f represents the Nyquist plots of the three supercapacitor devices (NCO/G–C, NCO/A–C, and NCO/A–G) measured in the frequency range of 0.1 Hz–100 kHz under 3 M KOH electrolyte. In order to understand the charge transfer characteristics of the cell, the EIS measurement was carried out before and after all the electrochemical studies, as shown in Fig. S5 in the ESI.† Note that the imaginary part of the impedance (Z'') raises abruptly in the low-frequency region, which is largely attributed to the ideal capacitive characteristics. The magnified part of the impedance response at the high-frequency region (inset of Fig. 5f) shows the semicircular patterns, evidencing the presence of bulk resistance and charge-transfer resistance at the electrode–electrolyte interfaces of the cells. It is obvious that the semicircular pattern is relatively higher in the NCO/G–C. The bulk resistance (R_b) and the charge transfer resistance at the interfaces (R_{ct}) of the capacitor were found from the incepts of the real-axis impedance values and by fitting with an equivalent circuit model, as shown in Fig. S5 in the ESI.† The obtained values of these parameters are shown in Table S2 in the ESI.† To fabricate high-performance supercapacitors for pulse power applications, the high rate capability of electrolytic ions due to shorter ionic diffusion pathways plays a significant role.[55] It enables faster ionic switching between the electrode and the electrolyte, leading to a possible faradaic process for enhanced and stable capacitance characteristics. The faster faradaic reaction process by means of the response time (τ_0) was estimated using the EIS data of the NCOs.[56,57] The Miller's approach is considered in order to evaluate the τ_0, which is the reciprocal of the response frequency obtained from Bode's plots.[58]

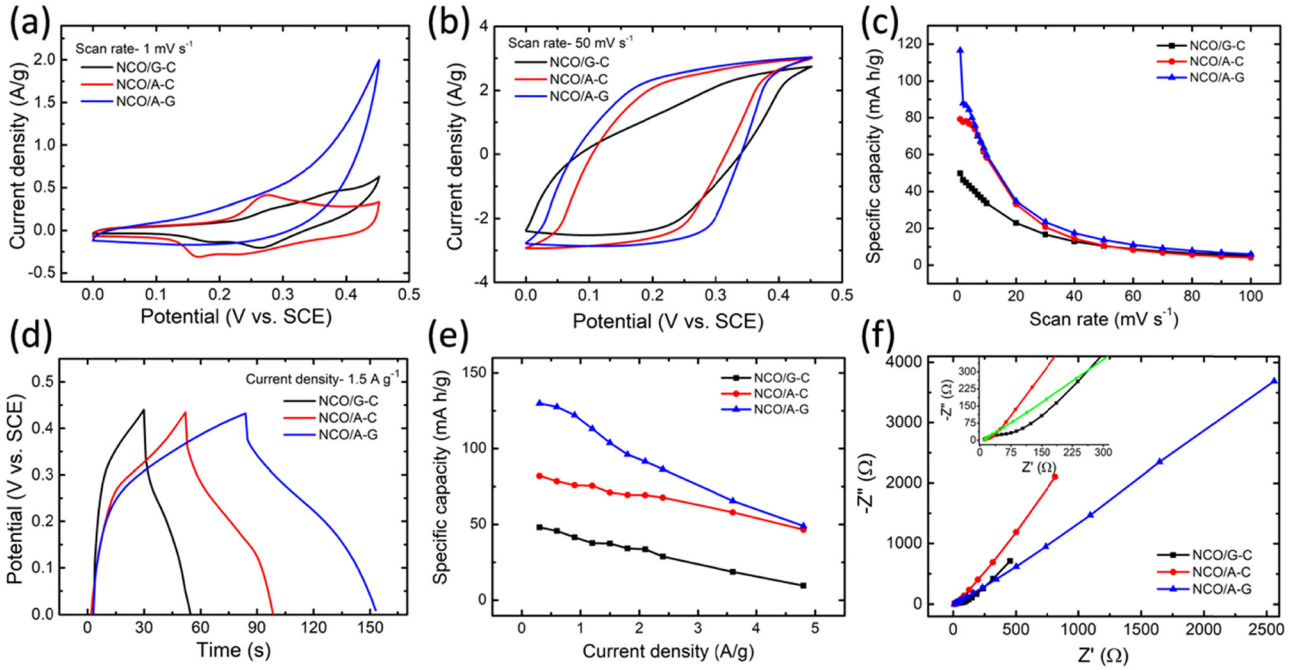

Fig. 5 CV curves of the NCO/G–C, NCO/A–C, and NCO/A–G obtained at the sweep rates of (a) 1 mV s^{-1} and (b) 50 mV s^{-1}, (c) scan rate dependent specific capacity plot, (d) GCD plots at a current density of 1.5 A g^{-1}, (e) the corresponding specific capacity plots at different discharge current densities, and (f) Nyquist plots of all NCO-based electrodes in 3 M KOH solution (inset is the magnified view).

Fig. S6 in the ESI† illustrates Bode's plots of the NCOs obtained from EIS analysis. The response frequencies, in which the Z' and Z'' are reflected equally, and the corresponding response times were evaluated from the frequency *vs.* Z' or Z'' plot (Fig. S6 in ESI†) for estimating the rate capability of the devices. The relatively smallest value ($\sim$0.008 s) of τ_0 has been obtained for NCO/A–G, as compared to that of the NCO/A–C (0.034 s) and NCO/G–C (0.089 s), indicating that the electrolytic ions possess faster switching characteristics through the electrode–electrolyte interface (Table S2 of ESI†).[58] Therefore, the NCO/A–G exhibited a rectangular cyclic pattern in the CV curves with the disappearance of the redox patterns.

3.4. Electrochemical performance of the all-solid-state ASC

In order to validate the practical applicability of the structural and morphologically tuned NCO, we have fabricated an all-solid-state ASC. Based on the better electrochemical performance resulting from the NCOs, the NCO/A–G sheet-like nanostructure has been chosen to construct the real ASC. In a way, the ASC comprised an NCO/A–G sheet-like nanostructure as an active material (cathode), PVA–KOH as the solid electrolyte, and carbon black super-P as the anode electrode. Prior to starting the electrochemical analysis, the active masses of both the cathode and anode were optimized for balancing the charge on both sides. The CV, GCD, and EIS studies were carried out to understand the capacitance behaviors of the ASC device, as shown in Fig. 6. The CV measurements with different potential windows (0–1 V, 0–1.5 V, and 0–2.0 V) and scan rates (5–70 mV s^{-1}) were performed for ASC operation (Fig. 6a and b). In both the cases of NCO/A–G-based ASC, the CV curves appeared to be a constant quasi-rectangular shape due to the EDL formation, which is an essential characteristic in supercapacitors, suggesting the high rate capability, low equivalent series resistance (ESR), and hence faster charge–discharge property. The GCD profiles studied at different current densities (0.2–1.0 mA cm^{-2}) with a potential window of 0–1.5 V exhibit an almost symmetric nature, indicating the better electrochemical reversibility of the ASC (Fig. 6c). The areal capacitance (C_a) of the ASC device is estimated using the GCD profiles (Fig. 6d). The value of C_a decreases with an increase in current density. The difference in C_a values as the variation of current density is almost 4-fold higher, demonstrating the good performance of ASC at a higher current density.

To further determine the performance of NCO/A–G-based ASC, the Ragone plot is presented in Fig. 6e. The Ragone plot denotes the relationship between the energy density (E_d) and power density (P_d) obtained from the GCD profiles. In this work, the NCO/A–G-based ASC device exhibits an energy density of 8.5 μW h cm^{-2} at a power density of 400 μW cm^{-2}, and 3.8 μW h cm^{-2} at a higher power density of 1950 μW cm^{-2}. The long-term cycling capability of the NCO/A–G-based ASC device was studied using a GCD test under 7000 continuous cycles at a constant current density of 0.6 mA cm^{-2} (Fig. 6f). Both the capacitance retention and Coulombic efficiency displayed a value of nearly 90% over 7000 cycles. To further demonstrate the high-energy performance, initially, the six assembled NCO/A–G-based ASC devices are connected in series and charged at approximately 6.5 V. In the subsequent discharging, the devices are connected with a blue LED (2.1 V, 80 mW), and these devices are capable of lighting a LED for more than 5 min (the corresponding real-time movie can be seen in Movie S1 in

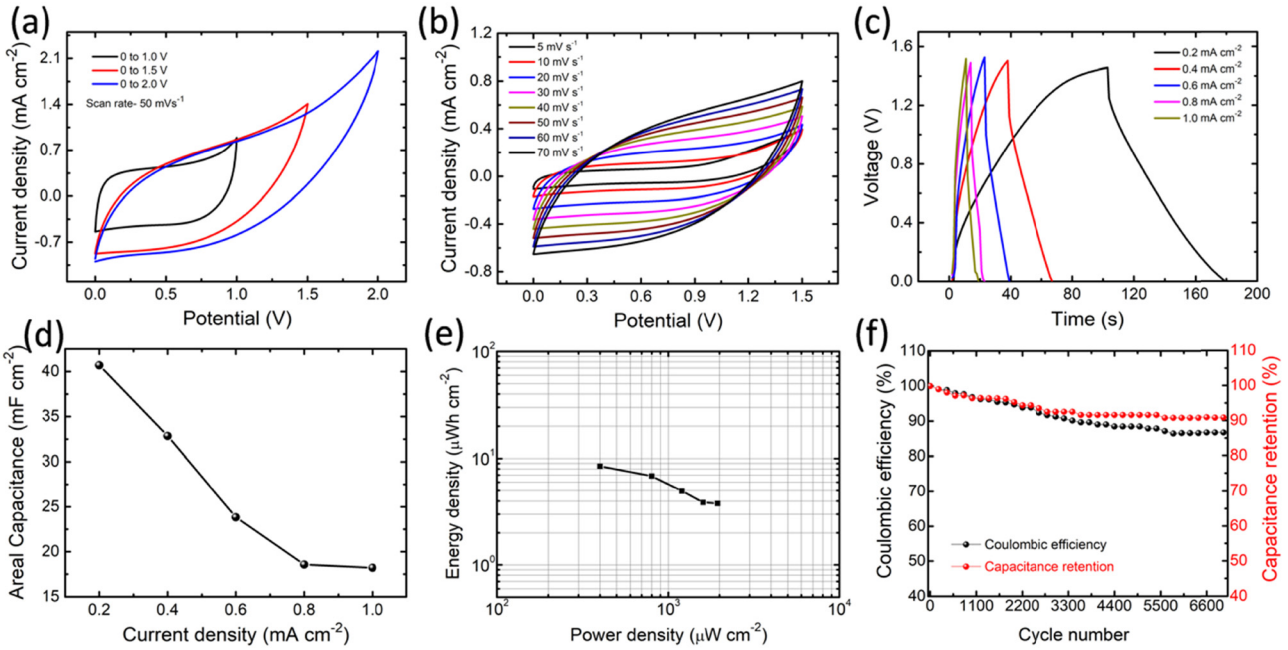

Fig. 6 NCO/A–G-based ASC measurements: CV curves with (a) different potential windows (0–1 V, 0–1.5 V, and 0–2.0 V), (b) scan rates (5–70 mV s^{-1}), (c) GCD plots with various current densities (0.2–1.0 mA cm^{-2}), (d) the corresponding areal capacitance (C_a) at different discharge current densities, (e) Ragone plot, and (f) capacitance retention as a function of charge–discharge cycles.

the ESI†). This suggests that the NCO/A–G-based ASC devices possess high-energy storage capacity. Moreover, to ensure the charge transport characteristics of the ASC device, the EIS study was performed before and after all the electrochemical studies, as shown in Fig. S7 in the ESI.† The Nyquist plots show almost similar patterns after all the electrochemical studies were performed as compared to that of the pristine state. Furthermore, based on the impedance investigation (Table S2 in ESI†), we have confirmed a lower range of response time (τ_0) and a higher value of response frequency (f_0). This infers that the electrolytic ions possess faster intercalation/de-intercalation (switching) kinetics in the electrode–electrolyte interfaces.[59] As a consequence, a pseudo-rectangular CV behavior and higher value of capacitance are obtained because of the fast-reversible faradaic reactions.

4. Conclusions

In summary, the morphologically tuned NCO nanostructures have been synthesized by various combinations of nucleobases during preparation. Owing to the large variations in the metal-coordination properties of adenine and guanine, the NCO/A–G unveils entirely different morphological features relative to that of the remaining materials. Among all three NCOs, the NCO/A–G with sheet-like nanostructures reveals the quasi-rectangular shape of the CV curves, interpreted by the EDL capacitance behavior of the cell. Significantly, the absence of redox behavior by various measuring parameters indicates that the NCO/A–G-based electrode is promising for use in ultrafast redox reactions. In particular, a very low response time (τ_0) and higher response frequency (f_0) in the impedance pattern confirm that the NCO/A–G-based nanostructures have faster switching kinetics of electrolytic ions in the electrode–electrolyte interface. The NCO/A–G-based ASC device shows an energy density of 3.8 μW h cm^{-2} at a higher power density of 1950 μW cm^{-2}. Based on these results, it is speculated that synergistic tuning of the NCO nanostructures by the nucleobase combinations may open new opportunities for developing future energy storage systems.

Author contributions

All authors contributed to preparing the manuscript. The material preparation was done by SK. Several data collections were performed by AD. The device fabrication, interpretation, and manuscript design were performed by KK. The discussions on constructing the overall manuscript were done by KK, SK, and SV. All authors have validated the final manuscript for publication.

Conflicts of interest

The authors declare that they have no conflict of interest.

Acknowledgements

Dr KK would like to thank the Science and Engineering Research Board (SERB) and the Department of Science & Technology (DST), India for support to carry out this work under Early Career Research (ECR/2017/002615) and DST inspire faculty scheme (DST/INSPIRE/04/2016/000246).

References

1 K. Chena and D. Xue, Materials Chemistry Toward Electrochemical Energy Storage, *J. Mater. Chem. A*, 2016, **4**, 7522–7537.

2 E. Pomerantseva, F. Bonaccorso, X. Feng, Y. Cui and Y. Gogotsi, Energy Storage: The Future Enabled by Nanomaterials, *Science*, 2019, **366**, aan828.

3 J. Liu, J. Wang, C. Xu, H. Jiang, C. Li, L. Zhang, J. Lin and Z. X. Shen, Advanced Energy Storage Devices: Basic Principles, Analytical Methods, and Rational Materials Design, *Adv. Sci.*, 2017, **5**, 1700322.

4 J. R. Miller and P. Simon, Electrochemical Capacitors for Energy Management, *Science*, 2008, **321**, 651–652.

5 M. E. Şahin, F. Blaabjerg and A. Sangwongwanich, A Comprehensive Review on Supercapacitor Applications and Developments, *Energies*, 2022, **15**, 674–700.

6 A. C. Forse, C. Merlet, J. M. Griffin and C. P. Grey, New Perspectives on the Charging Mechanisms of Supercapacitors, *J. Am. Chem. Soc.*, 2016, **138**, 5731–5744.

7 H. Wang, H. S. Casalongue, Y. Liang and H. Dai, $Ni(OH)_2$ Nanoplates Grown on Graphene as Advanced Electrochemical Pseudocapacitor Materials, *J. Am. Chem. Soc.*, 2010, **132**, 7472–7477.

8 Y. Gogotsi and R. M. Penner, Energy Storage in Nanomaterials—Capacitive, Pseudocapacitive, or Battery-like?, *ACS Nano*, 2018, **12**, 2081–2083.

9 G. Wang, L. Zhang and J. Zhang, A review of Electrode Materials for Electrochemical Supercapacitors, *Chem. Soc. Rev.*, 2012, **41**, 797–828.

10 A. Abdisattar, M. Yeleuov, C. Daulbayev, K. Askaruly, A. Tolynbekov, A. Taurbekov and N. Prikhodko, Recent Advances and Challenges of Current Collectors for Supercapacitors, *Electrochem. Commun.*, 2022, **142**, 107373.

11 H. Banda, J. H. Dou, T. Chen, N. J. Libretto, M. Chaudhary, G. M. Bernard, J. T. Miller, V. K. Michaelis and M. Dincă, High-Capacitance Pseudocapacitors from Li^+ Ion Intercalation in Nonporous, Electrically Conductive 2D Coordination Polymers, *J. Am. Chem. Soc.*, 2021, **143**, 2285–2292.

12 D. Li, S. Yang, X. Chen, W. Y. Lai and W. Huang, 3D Wearable Fabric-Based Micro-Supercapacitors with Ultra-High Areal Capacitance, *Adv. Funct. Mater.*, 2021, **31**, 2107484.

13 K. Krishnan, P. Jayaraman, S. Balasubramanian and U. Mani, Nanoionic Transport and Electric Double Layer Formation at the Electrode/Polymer Interface for High-Performance Supercapacitors, *J. Mater. Chem. A*, 2018, **6**, 23650–23658.

14 *Metal Oxides in Energy Technologies*, ed. Y. Wu, Elsevier Inc., New York, 1st edn, 2018.

15 C. An, Y. Zhang, H. Guo and Y. Wang, Metal Oxide-Based Supercapacitors: Progress and Prospectives, *Nanoscale Adv.*, 2019, **1**, 4644–4658.

16 T. Nguyen and M. de. Montemor, Metal Oxide and Hydroxide–Based Aqueous Supercapacitors: From Charge Storage Mechanisms and Functional Electrode Engineering to Need-Tailored Devices, *Adv. Sci.*, 2019, **6**, 1801797.

17 C. Wei, Q. Chen, C. Cheng, R. Liu, Q. Zhang and L. Zhang, Mesoporous Nickel Cobalt Manganese Sulfide Yolk–Shell Hollow Spheres for High-Performance Electrochemical Energy Storage, *Inorg. Chem. Front.*, 2019, **6**, 1851–1860.

18 C. Wei, J. Sun, Y. Zhang, Y. Liu, Z. Guo, W. Du, L. Liu and Y. Zhang, Hierarchical $Ni(OH)_2$–MnO_2 Hollow Spheres as an Electrode Material for High-Performance Supercapacitors, *Inorg. Chem. Front.*, 2022, **9**, 3542–3551.

19 Z. Shi, Y. Liu, Y. Zhang, J. Sun, J. Zhang, C. Wei, W. Du, L. Liu and C. Cheng, Designed Synthesis of Yolk-Shelled $NiCo_2O_4$/$MnCo_2O_4$ Hollow Sphere with Boosted Performance for Supercapacitors, *Appl. Surf. Sci.*, 2023, **611**, 155758.

20 C. Wei, R. Zhang, X. Zheng, Q. Ru, Q. Chen, C. Cui, G. Li and D. Zhang, Hierarchical Porous $NiCo_2O_4$/CeO_2 Hybrid Materials for High Performance Supercapacitors, *Inorg. Chem. Front.*, 2018, **5**, 3126–3134.

21 Y. A. Kumar and H.-J. Kim, Enhanced Electrochemical Performance of Nanoplate Nickel Cobaltite ($NiCo_2O_4$) Supercapacitor Applications, *RSC Adv.*, 2019, **9**, 1115–1122.

22 Y. A. Kumar and H.-J. Kim, Effect of Time on a Hierarchical Corn Skeleton-Like Composite of CoO@ZnO as Capacitive Electrode Material for High Specific Performance Supercapacitors, *Energies*, 2018, **11**, 3285.

23 M. Moniruzzaman, Y. A. Kumar, M. R. Pallavolu, H. M. Arbi, S. Alzahmi and I. M. Obaidat, Two-Dimensional Core–Shell Structure of Cobalt-Doped@MnO_2 Nanosheets Grown on Nickel Foam as a Binder-Free Battery-Type Electrode for Supercapacitor Application, *Nanomaterials*, 2022, **12**, 3187.

24 J.-H. Yoon, Y. A. Kumar, S. Sambasivam, S. A. Hira, T. N. V. Krishna, K. Zeb, W. Uddin, K. D. Kumar, I. M. Obaidat, S. Kim and H.-J. Kim, Highly Efficient Copper-Cobalt Sulfide Nano-Reeds Array with Simplistic Fabrication Strategy for Battery-Type Supercapacitors, *J. Energy Storage*, 2020, **32**, 101988.

25 Y. A. Kumar, G. Mani, M. R. Pallavolu, S. Sambasivam, R. R. Nallapureddy, M. Selvaraj and M. Alfakeer, A. A. A. Bahajjaj. M. Ouladsmane, S. S. Rao and S. Ramakrishnaa, Facile Synthesis of Efficient Construction of Tungsten Disulfide/Iron Cobaltite Nanocomposite Grown on Nickel Foam as a Battery-Type Energy Material for Electrochemical Supercapacitors with Superior Performance, *J. Colloid Interface Sci.*, 2022, **609**, 434–446.

26 P. F. Hu, D. P. Zhao, H. Q. Liu, K. F. Chen and X. Xu, Engineering PPy decorated $MnCo_2O_4$ Urchins for Quasi-solid-state Hybrid Capacitors, *CrystEngComm*, 2019, **21**, 1600–1606.

27 S. M. Babulal, K. Venkatesh, T. W. Chen, S. W. Chen, A. Krishnapandi, S. P. Rwei and S. K. Ramaraj, Synthesis of $MnMoO_4$ Nanorods by a Simple Co-Precipitation Method in Presence of Polyethylene Glycol for Pseudocapacitor Application, *Int. J. Electrochem. Sci.*, 2020, **15**, 7053–7063.

28 R. Liang, Y. Du, P. Xiao, J. Cheng, S. Yuan, Y. Chen, J. Yuan and J. Chen, Transition Metal Oxide Electrode Materials for Supercapacitors: A Review of Recent Developments, *Nanomaterials*, 2021, **11**, 1248.

29 D. S. Sun, Y. H. Li, Z. Y. Wang, X. P. Cheng, S. Jaffer and Y. F. Zhang, Understanding the Mechanism of Hydrogenated $NiCo_2O_4$ Nanograss Supported on Ni Foam for Enhanced-Performance Supercapacitors, *J. Mater. Chem. A*, 2016, **4**, 5198–5204.

30 C. Wang, E. Zhou, W. He, X. Deng, J. Huang, M. Ding, X. Wei, X. Liu and X. Xu, $NiCo_2O_4$-Based Supercapacitor Nanomaterials, *Nanomaterials*, 2017, **7**, 41.

31 Y. Lia, X. Hana, T. Yi, Y. He and X. Li, Review and Prospect of $NiCo_2O_4$-Based Composite Materials for Supercapacitor Electrodes, *J. Energy Chem.*, 2019, **31**, 54–78.

32 Y. R. Zhu, Z. B. Wu, M. J. Jing, H. S. Hou, Y. C. Yang, Y. Zhang, X. M. Yang, W. X. Song, X. N. Jia and X. B. Ji, Porous $NiCo_2O_4$ Spheres, Tuned through Carbon Quantum Dots Utilised as Advanced Materials for an Asymmetric Supercapacitor, *J. Mater. Chem. A*, 2015, **3**, 866–877.

33 X. Li, Y. Liu, Z. Jin, P. Li, X. Chen and D. Xiao, Enhanced Electrochemical Performance of C–NiO/$NiCo_2O_4$//AC Asymmetric Supercapacitor Based on Material Design and Device Exploration, *Electrochim. Acta*, 2019, **296**, 335–344.

34 D. Yan, W. Wang, X. Luo, C. Chen, Y. Zeng and Z. H. Zhu, $NiCo_2O_4$ with Oxygen Vacancies as Better Performance Electrode Material for Supercapacitor, *Chem. Eng. J.*, 2018, **334**, 864–872.

35 H. Hu, B. Guan, B. Xia and X. W. (David) Lou, Designed Formation of Co_3O_4/$NiCo_2O_4$ Double-Shelled Nanocages with Enhanced Pseudocapacitive and Electrocatalytic Properties, *J. Am. Chem. Soc.*, 2015, **137**, 5590–5595.

36 Z. Luo, D. Shu, F. Yi, J. Ling, M. Wang, C. Huanga and A. Gao, Hollow Urchin-Like $NiCo_2O_4$ Microspheres with Oxygen Vacancies Synthesized by Self-Template for Supercapacitors, *New J. Chem.*, 2021, **45**, 22748–22757.

37 L. V. Arsenie, V. Ladmiral, P. L. Desmazes and S. Catrouillet, Nucleobase-Containing Polymer Architectures Controlled by Supramolecular Interactions: The Key to Achieve Biomimetic Platforms with Various Morphologies, *Polym. Chem.*, 2022, **13**, 5798–5810.

38 F. Huq and M. C. R. Peter, Interaction between $NiCl_2$, and Nucleobases, Nucleosides and Nucleotides, *J. Inorg. Biochem.*, 2000, **78**, 217–226.

39 K. Hassanein, F. Zamora, O. Castillo and P. A. Ochoa, Supramolecular Interactions in Cobalt(II)–Nucleobases Complexes: A Methyl Matter, *Inorg. Chim. Acta*, 2016, **452**, 251–257.

40 Y. A. Kumar, K. D. Kumar and H.-J. Kim, Facile Preparation of A Highly Efficient NiZn2O4–NiO Nanoflower Composite Grown on Ni Foam as an Advanced Battery-Type Electrode Material For High-Performance Electrochemical Supercapacitors, *Dalton Trans.*, 2020, **49**, 3622–3629.

41 Y.-S. Lee, Y. A. Kumar, S. Sambasivam, S. A. Hira, K. Zeb, W. Uddin, P. R. S. Reddy, K. D. Kumar, I. M. Obaidat, H.-J. Kim and S. Kim, $CoCu_2O_4$ Nanoflowers Architecture as an Electrode Material for Battery Type Supercapacitor with Improved Electrochemical Performance, *Nano-Struct. Nano-Objects*, 2020, **24**, 100618.

42 Y. He, L. Xu, Y. Zhai, A. Lia and X. Chen, A Hexangular Ring–Core $NiCo_2O_4$ Porous Nanosheet/NiO Nanoparticle Composite as an Advanced Anode Material for LIBs and Catalyst for CO Oxidation Applications, *Chem. Commun.*, 2015, **51**, 14768–14771.

43 P. Wu, S. Cheng, M. Yao, L. Yang, Y. Zhu, P. Liu, O. Xing, J. Zhou, M. Wang, H. Luo and M. Liu, A Low-Cost, Self-Standing $NiCo_2O_4$@CNT/CNT Multilayer, Electrode for Flexible Asymmetric Solid-State Supercapacitors, *Adv. Funct. Mater.*, 2017, 1702160.

44 R. C. Visvanathan and N. Ponpandian, $NiCo_2O_4$ Nanoparticles Inlaid on Sulphur and Nitrogen Doped and Co-doped rGO Sheets as Efficient Electrocatalysts for the Oxygen Evolution and Methanol Oxidation Reactions, *Nanoscale Adv.*, 2021, **3**, 3216–3231.

45 Y. A. Kumar and H.-J. Kim, Wearable Super-High Specific Performance Supercapacitors Using a Honeycomb with Folded Silk-Like Composite of $NiCo_2O_4$ Nanoplates Decorated with NiMoO4 Honeycombs On Nickel Foam, *Dalton Trans.*, 2018, **47**, 15545–15554.

46 Y. A. Kumar and H.-J. Kim, Preparation and Electrochemical Performance of $NiCo_2O_4$@$NiCo_2O_4$ Composite Nanoplates for High Performance Supercapacitor Applications, *New J. Chem.*, 2018, **42**, 19971–19978.

47 Y. A. Kumar, S. Singh, K. D. Kumar and H.-J. Kim, A $MoNiO_4$ Flower-Like Electrode Material for Enhanced Electrochemical Properties *via* a Facile Chemical Bath Deposition Method for Supercapacitor Applications, *New J. Chem.*, 2020, **44**, 522–529.

48 Y. A. Kumar, B. A. A. Asbahi, M. R. Pallavolu, S. S. Rao, R. R. Nallapureddy and S. Ramakrishna, Multiple Structural Defects in Poor Crystalline Nickel-Doped Tungsten Disulfide Nanorods Remarkably Enhance Supercapacitive Performance, *Int. J. Energy Res.*, 2022, **46**, 14227–14239.

49 Y. A. Kumar, K. D. Kumar and H.-J. Kim, Reagents Assisted $ZnCo_2O_4$ Nanomaterial for Supercapacitor Application, *Electrochim. Acta*, 2019, **330**, 135261.

50 H.-J. Kim, B. Naresh, I.-H. Cho, J.-S. Bak, S. A. Hira, P. R. S. Reddy, T. N. V. Krishna, K. D. Kumar, B. A. Mola and Y. A. Kumar, An Advanced Nano-Sticks & Flake-Type Architecture of Manganese-Cobalt Oxide as an Effective Electrode Material for Supercapacitor Applications, *J. Energy Storage*, 2021, **40**, 102702.

51 L. Shen, L. Yu, X. Yu, X. Zhang and X. Lou, Self-Templated Formation of Uniform $NiCo_2O_4$ hollow Spheres with Complex Interior Structures for Lithium-Ion Batteries and Supercapacitors, *Angew. Chem., Int. Ed.*, 2015, **54**, 1868–1872.

52 Z. Wu, Y. Zhu and X. Ji, $NiCo_2O_4$-Based Materials for Electrochemical Supercapacitors, *J. Mater. Chem. A*, 2014, **2**, 14759–14772.

53 X. Zhang, F. Yang, H. Chen, K. Wang, J. Chen, Y. Wang and S. Song, In Situ Growth of 2D Ultrathin $NiCo_2O_4$ Nanosheet Arrays on Ni Foam for High Performance and Flexible Solid-State Supercapacitors, *Small*, 2020, **16**, 2004188.

54 L. Kumar, H. Chauhan, N. Yadav, N. Yadav, S. A. Hashmi and S. Deka, Faster Ion Switching $NiCo_2O_4$ Nanoparticle Electrode-Based Supercapacitor Device with High

Performances and Long Cycling Stability, *ACS Appl. Energy Mater.*, 2018, **1**, 6999–7006.

55 M. Beidaghi and Y. Gogotsi, Capacitive Energy Storage in Micro-Scale Devices: Recent Advances in Design and Fabrication of Micro-Supercapacitors, *Energy Environ. Sci.*, 2014, **7**, 867–884.

56 M. K. Singh, M. Suleman, Y. Kumar and S. A. Hashmi, A Novel Configuration of Electrical Double Layer Capacitor with Plastic Crystal Based Gel Polymer Electrolyte and Graphene Nano-Platelets as Electrodes: A High Rate Performance, *Energy*, 2015, **80**, 465–473.

57 J. R. Miller, In Proceedings of the 8th International Seminar on Double Layer Capacitor and Similar Energy Storage Devices, Deerfield Beach, Florida, December 7–9, 1998; Ed. S. P. Wolsky, Florida Educational Seminars: Boca Raton, FL, 1998.

58 H. Chauhan, M. K. Singh, P. Kumar, S. A. Hashmi and S. Deka, Development of SnS_2/RGO Nanosheet Composite for Cost-Effective Aqueous Hybrid Supercapacitors, *Nanotechnology*, 2017, **28**, 025401.

59 P. Tamilarasan and S. Ramaprabhu, Graphene Based All-Solid-State Supercapacitors with Ionic Liquid Incorporated Polyacrylonitrile Electrolyte, *Energy*, 2013, **51**, 374–381.